Research Article Vol. 30, No. 5 / 28 Feb 2022 / Optics Express 7342
Optics EXPRESS

Coherent generation of arbitrary first-order Poincaré sphere beams on an Si chip

HAILONG PI,[1] WANGKE YU,[1] JIZE YAN,[1,2] AND XU FANG[1,3]

[1]School of Electronics and Computer Science, University of Southampton, SO17 1BJ, UK
[2]J.Yan@soton.ac.uk
[3]x.fang@soton.ac.uk

Abstract: Generalized vector vortex light beams possess spatially variant polarization states, and higher-order Poincaré spheres represent a powerful analytical tool for analyzing these intriguing and complicated optical fields. For the generation of these vortex beams, a range of different methods have been explored, with an increasing emphasis placed on compact, integrated devices. Here, we demonstrate via numerical simulation, for the first time, an on-chip light emitter that allows for the controllable generation of all points on a first-order Poincaré sphere (FOPS). The FOPS beam generator consists of a waveguide-coupled, nanostructured Si microring resonator that converts two guided, coherent light waves into freely propagating output light. By matching their whispering gallery modes with the nanostructures, the fundamental TE (transverse electric) and TM (transverse magnetic) input modes produce radial and azimuthal polarizations, respectively. These two linear polarizations can form a pair of eigenstates for the FOPS. Consequently, tuning the phase contrast and the intensity ratio of these two coherent inputs allows for the generation of an arbitrary point on the FOPS. This result indicates a new way for on-chip vector vortex beam generation, which may be applied for integrated optical tweezers and high-capacity optical communications.

1. Introduction

Generalized vector vortex beams are a type of light beam that possesses spatially variant polarization states, where the light polarization on the beam cross section varies with the location with respect to the beam axis [1]. These unique polarization states have triggered tremendous research interests, leading to a wide range of potential applications including high-resolution imaging [2,3], laser micromachining [4,5], optical tweezers [6,7], classical optical communications [8,9], and quantum communications [10,11]. Nevertheless, as compared to the conventional plane wave that possesses a single, uniform polarization state, the generalized vector vortex beams are much more difficult to understand and analyze. In order to address this challenge, the concept of higher-order Poincaré spheres was developed [12], which has since been proved to be a convenient and powerful analytical tool. Each higher-order Poincaré sphere represents a set of polarization states, each corresponding to a unique point on the sphere. This geometric representation provides an intuitive interpretation of these intriguing polarization states, and is useful for analyzing light generation and transformation.

As an example, the first-order Poincaré sphere (FOPS) [12] has a north pole where the spin angular momentum and the orbital angular momentum (OAM) are $\hbar$ and $-\hbar$, respectively, and a south pole with the corresponding values swapped to $-\hbar$ and $\hbar$, where $\hbar$ is the reduced Planck constant. These two polarization states represent two vortex beams, or more specifically scalar vortex beams [13], that carry a finite topological charge. The polarization across the beam cross section is uniformly circular, only with its phase modulated azimuthally by the finite topological charge. By comparison, the polarization states on the equator of the FOPS carry no spin angular

#438695 https://doi.org/10.1364/OE.438695
Journal © 2022 Received 26 Jul 2021; revised 7 Dec 2021; accepted 8 Dec 2021; published 18 Feb 2022

Optics EXPRESS

momentum and OAM: they are all linear and possess cylindrical symmetry. Due to this cylindrical symmetry in polarization, these beams are termed as cylindrical vector beams [14]. Historically, the research on vortex beams used to focus exclusively on the study of topological charge, making it of little relevance to that on cylindrical vector beams. The concept of generalized vector vortex beam, which accommodates beams with both zero and a finite topological charge, establishes the conceptual links between these two research areas, consequently provides new insights into these unique optical fields.

This work concentrates on the on-chip generation of the polarization states on the FOPS. The vortex beams mentioned above, including the linearly (i.e. radially, azimuthally and spirally) polarized states on the equator of the FOPS and the circularly polarized beams at its two poles, are among the most studied vortex beams. Although these vortex beams have been explored individually without the support of the FOPS, their mutual transformation (i.e. creating a specific state by using one or multiple other states) greatly benefits from studying the FOPS. The FOPS beam generation and transformation have been achieved by using both intracavity [15,16] and extracavity methods. The latter contains a wide range of different approaches, including interferometric mixing [17,18], as well as direct conversion using optical elements such as liquid crystals [19–22], metasurfaces [23–25] and fibers [26]. These approaches often provide a high level of control on light polarization. Nevertheless, they cannot be easily combined with a photonic integrated circuit to enable large-scale, on-chip integration. In this regard, recent advances of integrated OAM light emitters, which share the basic configuration of a microring resonator embedded with an angular grating, represent a better solution [27–33]. In these light emitters, topological charge accompanies the on-chip light emission. Dynamical tuning of the OAM and the polarization states is a highly desired functionality for these light emitters. It has been achieved by tuning the input wavelength [27] and mode [30].

In this work, we expand the scope of integrated, tunable OAM light emitters, and demonstrate in numerical simulation an integrated FOPS beam emitter. As opposed to integrated OAM emitters reported previously [27–33], which generated only one or two point on the FOPS, the FOPS emitter analyzed here provides access to all the points on the FOPS. Without changing the input wavelength, the device can generate any polarization state on the FOPS, by balancing the transverse electric (TE) and the transverse magnetic (TM) input modes. To the best of our knowledge, this work represents the first demonstration of an on-chip light emitter that can generate any vortex beam on the FOPS.

2. Design schematic of the FOPS beam emitter

Figure 1 schematically illustrates the FOPS beam emitter. The device utilizes a silicon-on-insulator (SOI) platform, a common choice for on-chip light sources and photonic integrated circuits [34,35]. It consists of a Si microring resonator and a Si bus waveguide embedded inside a 4.3-μm thick layer of SiO_2, with the bottom of these two embedded components 2 μm above the Si substrate. Both components have a square cross section with a side length of 300 nm. The microring has a bend radius, defined as being from the inner boundary of the waveguide, of 5 μm, and a gap with the straight waveguide of 300 nm. The top of the microring is decorated with 35 shallow, cylindrical holes that distribute uniformly along the center of the waveguide. These holes have a depth of 100 nm and a diameter of 100 nm. They function as the grating elements for light out-coupling, converting confined waveguide modes to freely propagating output light.

The performance of the FOPS beam emitter was numerically evaluated by using a commercial FDTD (finite-difference time-domain) solver (Lumerical FDTD Solutions). A free-space wavelength range from 1658 nm to 1722 nm was simulated. The device was assumed to have zero light absorption in the whole range. The permittivity of Si and SiO_2 was obtained by fitting experimental measurement [36], and the values were 12.03 and 2.08, respectively, at the emitter working wavelength of $\lambda = 1685.59$ nm. The device was driven by the fundamental TE and TM

Optics EXPRESS

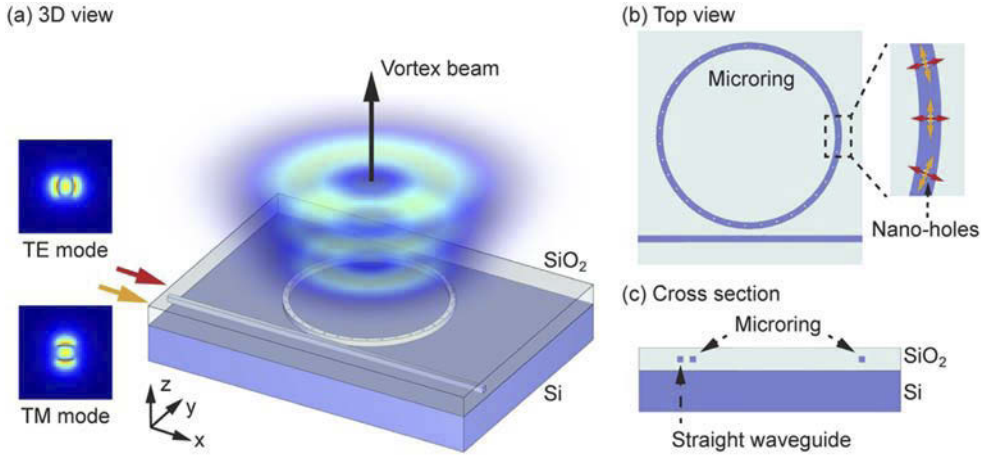

Fig. 1. Schematic of the FOPS beam emitter. (a) The emitter consists of a Si microring resonator evanescently coupled to a straight bus waveguide. Driven by the fundamental TE and TM modes fed into the bus waveguide, the microring radiates light into free space in the vertical direction. The polarization state of the output light is modulated by tuning the phase contrast and the intensity ratio of the two input modes, and it can sweep over the whole FOPS. (b) The microring is decorated on top with 35 uniformly distributed, shallow nano-holes that function as an angular grating for light out-coupling. The inset is a zoomed-in view of a section of the microring. The TE and TM input modes, which have the same wavelength, produce radially and azimuthally polarized components in the output beam, respectively. (c) Cross-sectional view of the device at the plane bisecting the microring.

modes of the bus waveguide, which were launched 6 μm away from the 300 nm gap (i.e. the location where the microring and the straight waveguide were the closest). In the following discussions, the phase contrast between the two coherent input modes always refers to this specific input plane. Nevertheless, as the TE and TM modes have almost identical effective indices (1.846068 versus 1.846072) due to the square shape of the cross section, the phase contrast in the straight waveguide is almost invariant as the two modes propagate forward, and the location of the input plane has no significant influence on the device characteristics.

3. Input mode-dependent microring resonances

Figure 2(a) shows the transmission spectra of the fundamental TE and TM modes propagating in the bus waveguide. Both spectra contain a series of sharp resonance dips, each corresponding to a whispering gallery mode (WGM) in the microring. In both spectra, the two closely spaced resonances dips between 1680 nm and 1700 nm form a resonance doublet. These doublets are characteristics of mode splitting caused by the coupling between counter-propagating WGMs inside the ring [37]. Both the singlet and doublet resonances occur at similar wavelengths for the two input modes. This similarity originates from the highly symmetric shape of the waveguide cross section (a square), as well as the uniformity of the embedding environment (i.e. both the straight and circular waveguides are fully covered with a SiO_2 layer). The differences between these two spectra are attributed to the asymmetry introduced by the microring-waveguide coupling region and the nano-hole top grating.

As will be discussed in details below, the FOPS beam generation requires both the TE WGM and the TM WGM to have an azimuthal order of 35, the same as the number of the grating elements (i.e. the nano-holes). This condition is satisfied only in the resonance doublet. To simplify the analysis, we further require the TE and TM inputs to have similar waveguide

Optics EXPRESS

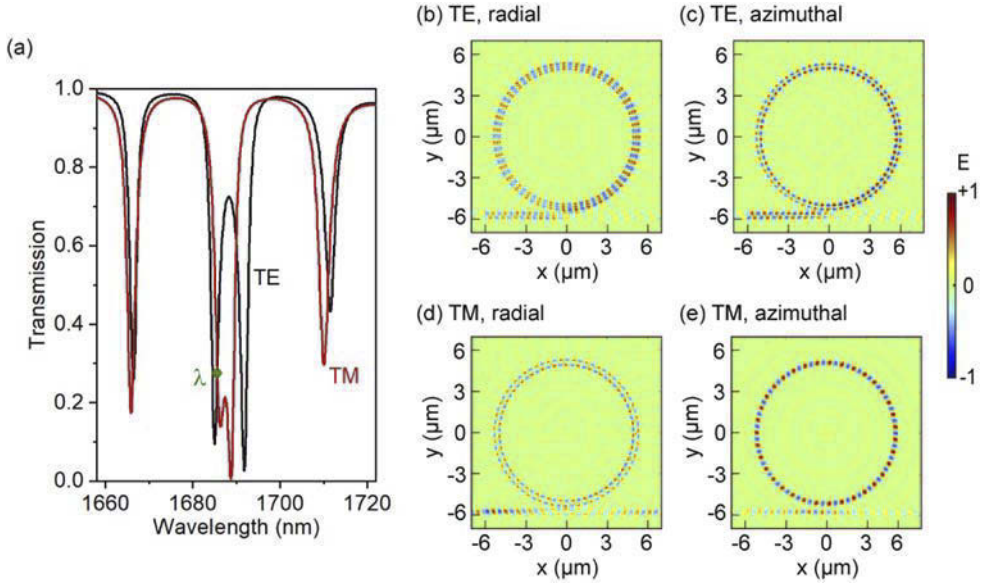

Fig. 2. Input and near-field properties of the FOPS beam emitter. (a) Transmission spectra of the TE and TM modes in the bus waveguide. The emitter working wavelength is λ=1685.59 nm (green spot). (b) The radial and (c) the azimuthal component of the electric field in the microring, with the microring driven only by the TE input mode. (d,e) Corresponding field components under the TM input. All the four maps show the same *xy* plane that passes through the middle height of the nano-holes.

transmission at the device working wavelength. The wavelength is consequently chosen as $\lambda = 1685.59$ nm, a wavelength in the resonance doublet where the TE and TM transmission is approximately equal to 0.28.

Figure 2(b)–2(e) show the electric near field at this wavelength for the two inputs. The results confirm that both inputs generate a WGM in the microring, and the WGM has an azimuthal order of the target value of 35. Despite this similarity in azimuthal order, the two WGMs are distinct in the details of field distribution. Most relevant to the light out-coupling is the field strength along the circumference passing the middle of the microring (i.e. the centers of the nano-holes). For the TE input, the field strength is almost zero for the azimuthal component. In contrast, for the TM input, it is the radial component that has nearly zero strength. This contrast between the azimuthal and radial components underpins our technique of arbitrary FOPS beam generation.

4. Vortex beam generation using a single input mode

Due to their different near-field distributions inside the microring, the TE and TM inputs generate two freely propagating light beams with distinct features. Figure 3 shows the intensity and phase distributions of these two output beams, analyzed at a radial distance of one meter from the device center. In the analysis, the radially (E_{RAD}) and azimuthally (E_{AZ}) polarized components are extracted [38] using the Jones vectors as below,

$$E = E_{RAD} + E_{AZ} = \sum\nolimits_l \Psi^l_{RAD} \exp(il\theta) \begin{bmatrix} cos\theta \\ sin\theta \end{bmatrix} + \sum\nolimits_l \Psi^l_{AZ} \exp(il\theta) \begin{bmatrix} -sin\theta \\ cos\theta \end{bmatrix} \quad (1)$$

Optics EXPRESS

where θ is the azimuthal angle and i is the unit imaginary number. l is the topological charge, and it is an integer (i.e. 0, ±1, ±2 etc.). Ψ^l_{RAD} is the coefficient for the radial component, which has an amplitude of $|\Psi^l_{RAD}|$ and a phase of ϕ^l_{RAD}, and Ψ^l_{AZ} is that for the azimuthal component.

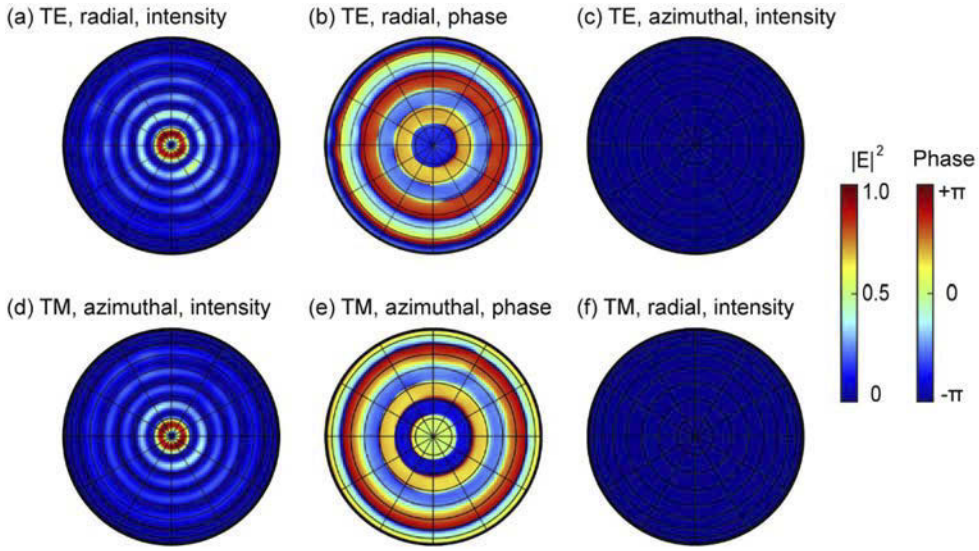

Fig. 3. Far-field radiation polar maps with the device driven by a single waveguide mode. (a-c) The intensity and phase distributions under the TE mode excitation. At the same intensity scale, (a) the radial component is clearly visible, while (c) the azimuthal component is indiscernible. (b) The phase of the dominant component (i.e. the radial component). (d-f) The corresponding intensity and phase distributions under the TM mode excitation. The phase is still for the dominant component, which is now the azimuthal component. The polarization is further visualized in Fig. 5.

Figure 3(a)–3(c) analyzes the output generated by a single TE input beam. The field is predominantly radially polarized: while the radial component shows clearly a set of concentric rings in its intensity distribution [Fig. 3(a)], the azimuthal component at the same intensity scale is not discernible [Fig. 3(c)]. Further analysis leads to an intensity ratio between the radial and the azimuthal components $|\Psi^l_{RAD}/\Psi^l_{AZ}|^2$, which can be expressed alternatively as I^l_{RAD}/I^l_{AZ}, of 98.56:1.44. The rings in Fig. 3(a) are slightly distorted and lack perfect rotational symmetry. This imperfection is attributed to the inhomogeneous field distribution inside the microring: the near-field amplitude has a noticeable decrease as the light traces the ring in the anti-clockwise direction from the microring-waveguide gap [Fig. 2(b)], creating a small variation among the 35 nano-holes in their light scattering strength. For all the intensity rings in Fig. 3(a), the phase stays constant [Fig. 3 (b)], implying that the vortex beam carries no topological charge. These results of Figs. 3(a)–3(c) lead to the conclusion that the output beam is a radially polarized cylindrical vector beam, which corresponds to a point on the equator of the FOPS.

Changing the input light from the TE mode to the TM mode profoundly changes the output [Figs. 3(d)–3(f)], and the azimuthally polarized component becomes the dominant component. The intensity ratio between the radial and the azimuthal components $|\Psi^l_{RAD}/\Psi^l_{AZ}|^2$ (equivalently I^l_{RAD}/I^l_{AZ}) now becomes 0.98:99.02. Despite this reverse in dominant component, many key features in the output are retained: the intensity distribution consists of a set of concentric rings [Fig. 3(d)], and the phase is invariant in each ring [Fig. 3(e)]. We can draw a similar conclusion here that, the output beam is now an azimuthally polarized cylindrical vector beam, which also corresponds to a point on the equator of the FOPS.

Optics EXPRESS

The phase distributions shown in Figs. 3(b) and 3(e) indicate that, both Ψ^l_{RAD} and are dominated by the term of l=0. For this reason, in the following discussions we omit the annotation of l unless it may cause confusion; Ψ^l_{RAD}, Ψ^l_{AZ}, ϕ^l_{RAD}, ϕ^l_{AZ}, I^l_{RAD} and I^l_{AZ} are simply written as Ψ_{RAD}, Ψ_{AZ}, ϕ_{RAD}, ϕ_{AZ}, I_{RAD} and I_{AZ}, respectively.

The results in Fig. 3 can be interpreted based on the near-field distribution inside the microring (Fig. 2). Each nano-hole on the microring functions as a nano-antenna that radiates the wave confined inside the microring into free space. For highly symmetric configurations, such as the azimuthally polarized and radially polarized waveguide modes scattered by a cylindrical nano-hole, the symmetry has to be preserved in light scattering [28]. This constraint implies that radial and azimuthal polarization components dominate the output for TE and TM inputs, respectively.

Although its polarization varies with the input, the output beam has a topological charge l that stays invariant between the TE and TM input modes. Regardless of the input mode, the output beam is always formed by the constructive interference of light scattered by all the nano-holes. Its topological charge l can be calculated by using the angular phase-matching condition [27] of

$$l = m - q \tag{2}$$

Here m is the azimuthal order of the resonance mode inside the microring (i.e. the cycle number of the WGM), and q is the number of the grating elements (i.e. the number of nano-holes). At the working wavelength of 1685.59 nm, the topological charge l is 0, as $m = q$=35 (Fig. 2). Based on the symmetry constraint specified above, along with the zero topological charge, we can conclude that, TE and TM inputs produce radially and azimuthally polarized cylindrical vector beams, respectively. This analytical conclusion fits with the numerical results in Fig. 3.

5. Stokes parameters for the FOPS

With two specific points (i.e. polarization states) on the FOPS equator produced, we discuss in the following sections the method to reach an arbitrary point on the FOPS. For any higher-order Poincaré sphere, the most common method of using two coherent beams to conduct such scans is to use circularly polarized light beams with opposite helicity (i.e. the two poles of the sphere) [15–18,20,23–26]. As far as we know, this is the only method that has been used in FOPS analysis. In contrast, here we highlight the fact that such superposition can utilize any orthogonal set of polarization states (i.e. any antipodal points on a sphere). This includes the radial and azimuthal polarization states shown in Fig. 3.

By using the radial and azimuthal polarizations as the basis (i.e. a set of orthonormal eigenstates) for the FOPS, the higher-order Stokes parameters are expressed as

$$S_0 = |\Psi_{RAD}|^2 + |\Psi_{AZ}|^2 = I_{RAD} + I_{AZ} \tag{3}$$

$$S_1 = |\Psi_{RAD}|^2 - |\Psi_{AZ}|^2 = I_{RAD} - I_{AZ} \tag{4}$$

$$S_2 = 2|\Psi_{RAD}||\Psi_{AZ}|\cos(\phi_{AZ} - \phi_{RAD}) = 2\sqrt{I_{RAD}I_{AZ}}\cos(\phi_{AZ} - \phi_{RAD}) \tag{5}$$

$$S_3 = 2|\Psi_{RAD}||\Psi_{AZ}|\sin(\phi_{AZ} - \phi_{RAD}) = 2\sqrt{I_{RAD}I_{AZ}}\sin(\phi_{AZ} - \phi_{RAD}) \tag{6}$$

It is worth noting that, these expressions are derived based on the Stokes parameters of a conventional Poincaré sphere using the linear polarization basis [39]; they are consequently different from the Stokes parameters of a FOPS using the circular polarization basis. It is always true that $|S_1|^2+|S_2|^2+|S_3|^2=|S_0|^2$. For simplicity, we set the total intensity S_0 as unity value in the following analysis, as all the beams are fully polarized. This implies that every point on the FOPS can be identified using a unique set of S_1, S_2 and S_3.

Based on the analysis above, we can see that the input intensity of the TE and TM modes (I_{TE} and I_{TM}) dominates the output intensity I_{RAD} and I_{AZ}, respectively, and their phase contrast

Optics EXPRESS

ϕ_{TM}-ϕ_{TE} determines the value of ϕ_{AZ}-ϕ_{RAD}. When the input contains both the TE and TM modes, the output polarization state is the coherent interference of the azimuthally and radially polarized components. This implies that I_{TE}, I_{TM}, ϕ_{TE} and ϕ_{TM} all influence the output. This influence is numerically evaluated in Figs. 4 and 5.

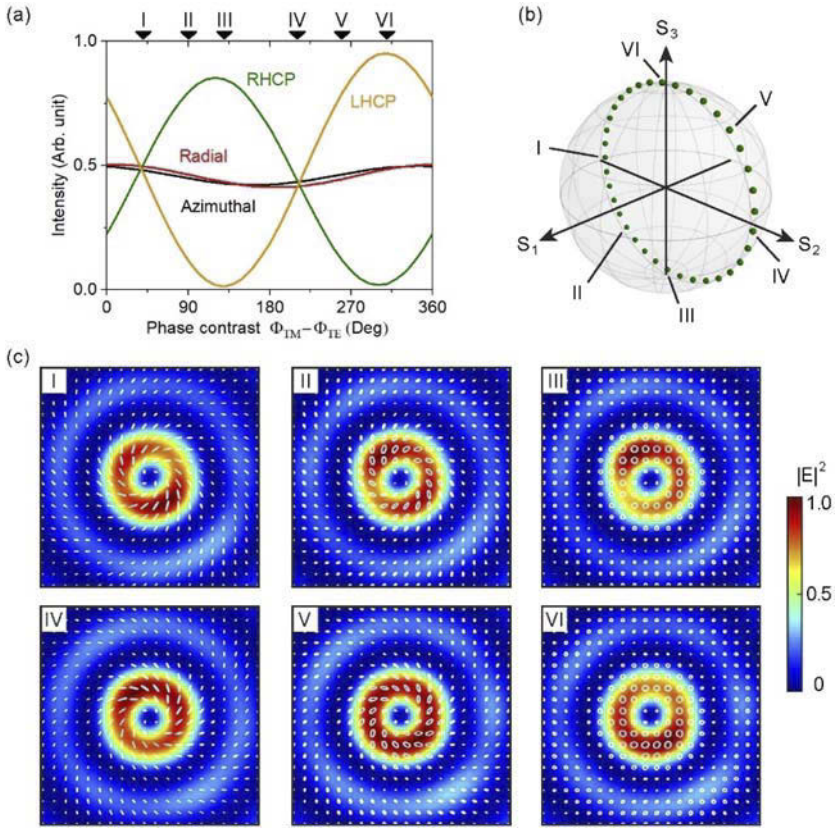

Fig. 4. Phase-controlled polarization evolution on the FOPS. (a) The output light is decomposed into radially and azimuthally polarized components, and alternatively into left-handed circularly polarized (LHCP) and right-handed circularly polarized (RHCP) components, as the input phase contrast ϕ_{TM}-ϕ_{TE} changes from 0° to 360°. Six representative ϕ_{TM}-ϕ_{TE} values (40°, 90°, 130°, 210°, 260° and 310°) are specified using numbers I to VI. (b) Polarization evolution on the FOPS beam (green dots) in the scan of the input phase contrast, with the six representative values specified. (c) The distributions of field intensity (color maps) and polarization (white ellipses and lines) for the six representative states. Each map corresponds to an area of 14 μm × 14 μm in the plane 20 μm above the top surface of the emitter. The intensity of each map is normalized against its respective maximum.

Optics EXPRESS

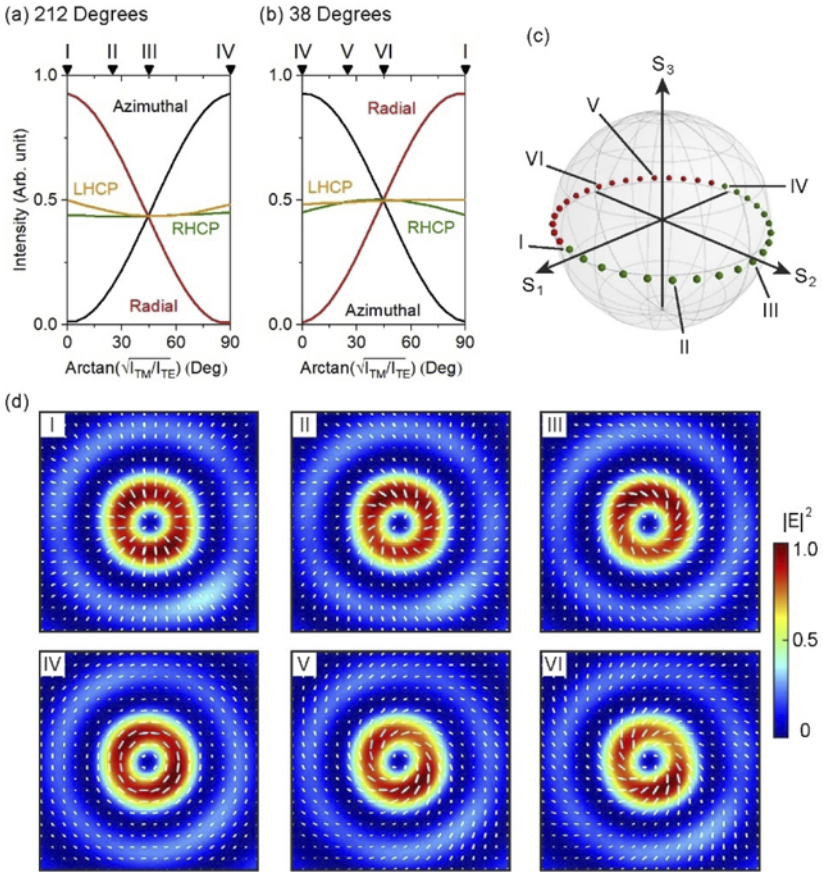

Fig. 5. Intensity-controlled polarized evolution on the FOPS. (a,b) Intensity decomposition using the linear basis (for the Azimuthal and Radial curves) and the circular polarization basis (for the RHCP and LHCP curves), as arctan $\left(\sqrt{I_{TM}/I_{TE}}\right)$ scans from 0° to 90°. The input phase contrast ϕ_{TM}-ϕ_{TE} is (a) 212° and (b) 38°. (c) The scan of arctan $\left(\sqrt{I_{TM}/I_{TE}}\right)$ shown in (a) and (b) produces polarization states that trace the equator. The green and red dots correspond to ϕ_{TM}-ϕ_{TE} at 212° and 38°, respectively. (c) The intensity and polarization distribution for the six representative states from I to VI. All the six panels are produced following the same method described in Fig. 4.

6. Longitudinal scan on the FOPS

Figure 4 shows the evolution of the output beam as the phase contrast of the two inputs ϕ_{TM}-ϕ_{TE} scans a full cycle of 360°. During the phase scan, the intensity ratio of the two inputs $I_{\mathrm{TE}}/I_{\mathrm{TM}}$ is set as a constant of 2.53. This value is identified by matching the total output intensity in Figs. 3(a) and 3(d), and is very close to creating the condition that the TE input and the TM input generate an equal amount of total output power. This ratio is not unity as might be predicted intuitively from Fig. 2(a), and it originates from the different field distributions of the two modes inside the waveguide [Figs. 2(b)–2(e), more analysis in Supplement 1]. At every phase contrast ϕ_{TM}-ϕ_{TE}, the output field is decomposed into the radially and azimuthally polarized components following Eq. (1), as well as into the left-handed and right-handed circularly polarized components (i.e. the two poles of the FOPS, here as E_{L} and E_{R}). The second type of decomposition is expressed as

Optics EXPRESS

[27,38]

$$E = E_L + E_R = \Psi_L^{-1} \exp(-i\theta)\frac{1}{\sqrt{2}}\begin{bmatrix} 1 \\ +i \end{bmatrix} + \Psi_R^{+1}\exp(i\theta)\frac{1}{\sqrt{2}}\begin{bmatrix} 1 \\ -i \end{bmatrix} \quad (7)$$

where Ψ_L^{-1} and Ψ_R^{+1} are the coefficients for the left-handed circularly polarized (LHCP) and right-handed circularly polarized (RHCP) components, respectively. It is worth highlighting that, the two circular components have finite and opposite topological charges (i.e. -1 and +1), which is different from the linear components.

Figure 4(a) shows the results of these two types of decomposition. As the TE and TM input modes generate predominantly radially and azimuthally polarized output light, respectively, the total output intensity is shared roughly equally between the radial and the azimuthal components throughout the 360° phase scan. Meanwhile, as the output is neither purely radial nor purely azimuthal for a single input mode (as discussed above, $I_{\mathrm{RAD}}/I_{\mathrm{AZ}}$ is 98.56:1.44 and 0.98:99.02 for purely TE and TM input, respectively), a low level of intensity interference exists in the output. It induces a small fluctuation in I_{RAD}, I_{AZ} and I_{RAD}+I_{AZ} in scanning ϕ_{TM}-ϕ_{TE}. In comparison to the linear basis, decomposing the output into circular polarizations shows a much bigger dependence on ϕ_{TM}-ϕ_{TE}: the ouput oscillates between almost purely left handed (at $I_{\mathrm{RHCP}}\approx 0$) to almost purely right handed (at $I_{\mathrm{LHCP}}\approx 0$).

The characteristics of I_{RAD}, I_{AZ}, I_{RHCP} and I_{LHCP} identified above lead to these two features related to the FOPS: (1) S_1=I_{RAD}-$I_{\mathrm{AZ}}\approx 0$ as ϕ_{TM}-ϕ_{TE} scans by 360°; (2) the two poles of the FOPS, which correspond to two pure circular polarization states, are reached in the scan. Based on these two features, we can predict that, the output polarization produced by a full 360° scan of ϕ_{TM}-ϕ_{TE} traces the great circle normal to the S_1 axis. This prediction is confirmed in more detailed analysis shown in Figs. 4(b) and 4(c).

At each ϕ_{TM}-ϕ_{TE}, the intensity distribution of the output light is similar to Figs. 3(a) and 3(d): it is a set of concentric rings, with most intensity concentrated in the smallest ring. As opposed to Fig. 4(a), which is based on the analysis of the total output intensity, we concentrate on the smallest ring for Fig. 4(b) and 4(c). Figure 4(c) shows both the intensity and the polarization distributions of this ring, with ϕ_{TM}-ϕ_{TE} taking six representative values of 40°, 90°, 130°, 210°, 260° and 310°. The doughty-shaped intensity distribution lacks perfect rotational symmetry, similar to the results shown in Fig. 3, and this imperfection is also present in the polarization distribution. To link these polarization maps with points on the FOPS, for each map, we compute the averaged polarization state along the circle that centers on the beam axis and passes the maximal intensity. This averaged polarization state is then identified on the FOPS in Fig. 4(b). This exercise is conducted for 36 values of ϕ_{TM}-ϕ_{TE}, from 0° to 360° at a step of 10°. Consistent with our prediction above, the polarization traces a great circle on the FOPS that is normal to the S_1 axis.

The great circle intersects with the equator at two points as seen in Fig. 4(b). As every point on the equator contains an equal amount of the polarization states at the two poles [12], these two points can be identified as the two points in Fig. 4(a) where the LHCP and the RHCP lines intersect. They correspond to ϕ_{TM}-ϕ_{TE} of 38° and 212°. These two values are important to the FOPS beam generation, and are to be used for the numerical simulation shown in Fig. 5.

Before concluding the analysis on the phase-based (i.e. tuning ϕ_{TM}-ϕ_{TE}) scan and starting that on the intensity-based (i.e. tuning $I_{\mathrm{TM}}/I_{\mathrm{TE}}$) scan (Fig. 5), it is worth analyzing briefly the imperfection seen in Fig. 4. In an ideal, perfect device that allows for the most straightforward control over the output polarization, as ϕ_{TM}-ϕ_{TE} changes steadily from 0° to 360°, the point on the FOPS would move longitudinally at a constant speed on a great circle. The device analyzed here slightly deviates from this ideal scenario, and the degree of deviation can be roughly gauged using a particular phase difference. As a numerical indication, here we use the two points where the great circle intersects the FOPS equator, which are discussed above. In the perfect device, the

Optics EXPRESS

phase difference between these two points is 180°. The discussion above shows that these two points correspond to ϕ_{TM}-ϕ_{TE} of 38° and 212° in Fig. 4(a), which have a difference of 174°. As benchmarked against the ideal device with regard to this parameter, our device drifts by a small value of 6°, or 3.3% in relative magnitude.

7. Latitudinal scan along the FOPS equator

In addition to the longitudinal scan on the FOPS shown in Fig. 4, it is also possible to conduct a horizontal scan along its equator (Fig. 5). Based on Eqs. (4)–(6), such polarization evolution can be achieved by adjusting S_1 and S_2, while maintaining S_3=0. The constraint on S_3 leads to two possible values of ϕ_{TM}-ϕ_{TE}, which are 38° and 212° as discussed above. Further analysis based on Eqs. (4)–(6) show that the value of arctan($|\Psi_{AZ}/\Psi_{RAD}|$), or expressed equivalently as arctan $\left(\sqrt{I_{AZ}/I_{RAD}}\right)$, is associated with the azimuthal position of the corresponding polarization state on the FOPS equator. This observation implies that the latitudinal scan can be achieved by tuning the input intensity ratio I_{TM}/I_{TE}, as it is proportional to the output ratio I_{AZ}/I_{RAD}.

Figure 5 analyzes this intensity-controlled FOPS scan. Figure 5(a) and 5(b) show the influence of the input intensity ratio on the four output components (azimuthal and radial components as a pair, and the two circular components as the other pair). Here the input variable is expressed as angle arctan $\left(\sqrt{I_{TM}/I_{TE}}\right)$, which ranges from 0° to 90°. Figure 5(c) shows that, as arctan $\left(\sqrt{I_{TM}/I_{TE}}\right)$ scans twice from 0° to 90°, with ϕ_{TM}-ϕ_{TE} first at 212° [Fig. 5(a)] and then at 38° [Fig. 5(b)], the polarization of the output beam evolves along the FOPS equator and eventually completes a full great circle of 360°. The two boundary arctan $\left(\sqrt{I_{TM}/I_{TE}}\right)$ values of 0° and 90° correspond to pure TE input and pure TM input, respectively, which are first analyzed in Fig. 3. Their polarization distributions shown in Fig. 5(d) fit well with the results derived from Fig. 3. Figure 5(d) also shows that, the four intermediate arctan $\left(\sqrt{I_{TM}/I_{TE}}\right)$ values (i.e. points II, III, V and VI) produce spiral polarizations. For these polarizations, the direction of twist is reversed once ϕ_{TM}-ϕ_{TE} changes between the two values of 212° (points II and III) and 38° (points V and VI).

8. Equations for arbitrary FOPS beam generation

The longitudinal and latitudinal scans shown respectively in Figs. 4 and 5 can be generalized to create any polarization state on the FOPS. This arbitrary FOPS beam generation relies on adjusting both input parameters, the intensity ratio I_{TM}/I_{TE} and the phase contrast ϕ_{TM}-ϕ_{TE}, simultaneously. Based on Eqs. (3)–(6), further assuming that TE and TM inputs generate respectively pure radial and azimuthal polarizations, these two input parameters can be derived from the three Stokes parameters as below

$$\frac{I_{TM}}{I_{TE}} = \eta\left|\frac{\Psi_{AZ}}{\Psi_{RAD}}\right|^2 = \eta\frac{S_2^2+S_3^2}{(S_1+1)^2} \tag{8}$$

$$\phi_{TM}-\phi_{TE} = \phi_{AZ}-\phi_{RAD}+\Omega = \arctan\left(\frac{S_3}{S_2}\right)+\left(1-\frac{S_2}{|S_2|}\right)\times 90^\circ+\Omega \tag{9}$$

Here, η=1/2.53 is the coefficient addressing the difference in the out-coupling efficiency of the TE and TM input modes (i.e. the TE input has to be 2.53 times as strong as the TM input, for the radially polarized output and the azimuthally polarized output to be equal in intensity). Ω=212° is one of the two angles used in the equator scan in Fig. 5. The term of (1-$S_2/|S_2|$)×90° is incorporated to create a 180° phase flip, so a single phase coefficient Ω is sufficient here, as opposed to the use of two values (i.e. 212° and 38°) in Fig. 5. This term takes the value of zero

Optics EXPRESS

at the singularity point of S_2=0. A key conclusion can be drawn here based on Eqs. (8) and (9) that, there exists a one-to-one correspondence between a pair of I_{TM}/I_{TE} and ϕ_{TM}-ϕ_{TE} values and a point on the FOPS.

Equations (8) and (9) are tested numerically using three sets of Stokes parameters that are chosen arbitrarily and listed in Table 1. The target Stokes parameters are inserted into the two equations to calculate the required input intensity ratio I_{TM}/I_{TE} and the phase contrast ϕ_{TM}-ϕ_{TE}. These two parameters are then used to conduct the numerical simulation, from which the output Stokes parameters are extracted. As seen in Table 1, the output Stokes parameters well reproduce the target values, with the maximal deviation as small as 0.09.

Table 1. Three points on the FOPS for testing the two equations on arbitrary FOPS beam generation. The two input parameters lead to output Stokes parameters that aim to replicate the target Stokes parameters. The term Intensity refers to the intensity ratio of I_{TM}/I_{TE}, and Phase to the phase contrast of ϕ_{TM}-ϕ_{TE}.

Test	Target			Coherent input		Output		
	S_1	S_2	S_3	Intensity	Phase (°)	S_1	S_2	S_3
I	0.707	0	0.707	0.068:1	302.00	0.661	0.004	0.749
II	-0.5	-0.707	0.5	1.186:1	356.73	-0.507	-0.653	0.561
III	0.577	0.577	-0.577	0.106:1	167.00	0.574	0.487	-0.655

Figure 6 shows the numerically simulated output at the three pairs of I_{TM}/I_{TE} and ϕ_{TM}-ϕ_{TE}, from which the output Stokes parameters listed in Table 1 are extracted. To provide a further comparison against the target polarizations and identify the source of the discrepancy, Fig. 6(a) shows corresponding analytical results derived from an ideal device. In the ideal device, the 35 nano-holes are assumed to be 35 identical, infinitesimal electric dipoles [40]. Regardless of the input, these dipoles always oscillate in phase to satisfy the angular phase-matching condition specified in Eq. (2). Each dipole has a radial component and an azimuthal component, with their relative intensity and phase contrast determined by Eqs. (8) and (9). As the analytical calculation leads to the ideal output beams seen in Fig. 6(a), we conclude here that the discrepancy between Figs. 6(a) and 6(b) mainly comes from the deviation of the nano-holes from ideal electric dipoles. It is expected that nano-holes with smaller dimensions can better approximate the ideal electric dipoles, albeit at the expense of reduced output efficiency.

For future optimization of this design, as well as for designs that can be derived from this work, we would like to highlight the scope of Eqs. (8) and (9). The only assumption used in their derivation is that the two fundamental input modes generate pure radial and azimuthal polarizations. Consequently, we believe that these two equations can be applied on any FOPS beam emitter that shares the basic configuration of our device (i.e. any FOPS beam emitter with an angular grating-integrated microring). The matching between the target and the actual polarization states depends on the matching between the grating element and the ideal electric dipole. If the embedded angular grating can be well approximated by a loop of identical, ideal electric dipoles, Eqs. (8) and (9) can lead to output polarizations that well match the target. For any specific design, the only free parameters are the two coefficients η and Ω, which can be determined following the approach described in Figs. 3 and 4.

Before concluding this work, it is worth recapitulating these two design principles for the FOPS emitter. The first one is that the TE and TM modes of the microring resonator need to have similar effective refractive indices. This constraint originates from Eq. (2), which requires the azimuthal order m to be identical for the two modes. Making the cross section of a fully embedded microring as a square, as in the example discussed here, is a straightforward solution. The other design principle is that the scatterers (nano-holes for the microring here) need to be relatively small. This requirement enables a good approximation to electrical dipoles for the scatterers (as in Fig. 6), as well as the formation of high-quality WGM in the microring (as in

Optics EXPRESS

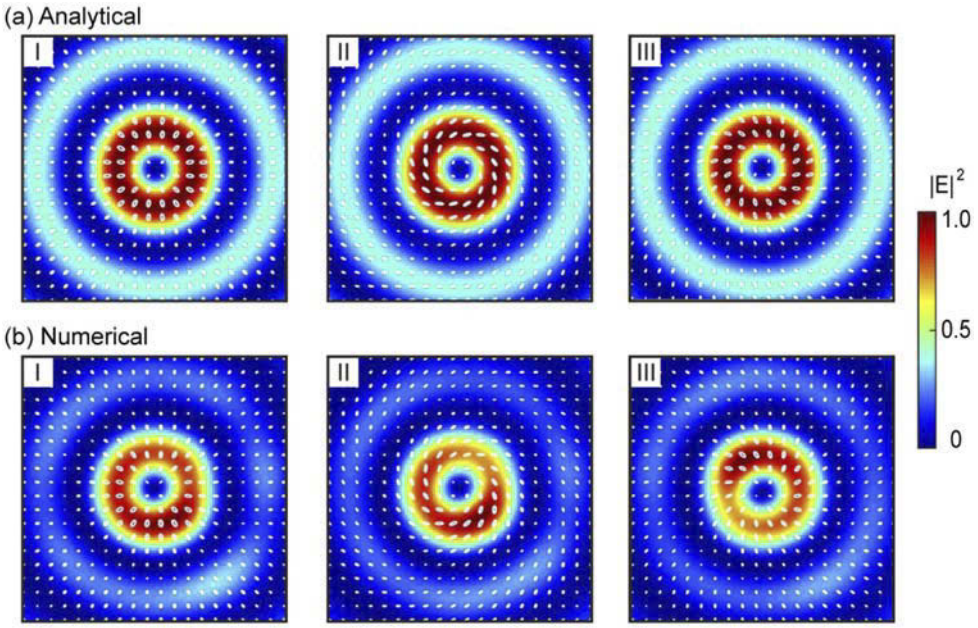

Fig. 6. Intensity and polarization distributions for the three test FOPS points listed in Table 1, with (a) the analytical results compared against (b) the numerical results. All the panels are produced following the same method described in Fig. 4.

Fig. 2). Nevertheless, a small scatterer size can adversely affect the emission efficiency. In the device here, only 12.08% of the TM input light is converted to the azimuthal component of the output light, and this emission efficiency further decreases to 4.78% for the generation of the radial component from the TE light.

9. Conclusion

To conclude, we have proposed and numerically analyzed a Si microring resonator-based FOPS beam emitter. As a special kind of integrated vortex beam generator, the FOPS emitter provides access to any point on the FOPS, in the vertically scattered light from the microring resonator. The microring is decorated on top with an angular grating of 35 nano-holes, and it evanescently couples to a Si bus waveguide. The nano-hole grating converts TE and TM waveguide modes into free space, as radially and azimuthally polarized cylindrical vector beams, respectively. By using these two linear polarizations as the basis, the Stokes parameters of the FOPS are derived. Based on these Stokes parameters, a method of producing arbitrary FOPS beams is established. The method utilizes simultaneous control over the relative phase and strength of the two input waveguide modes, and it is underpinned by the fact that there exists a one-to-one correspondence between a pair of these two input parameters and a point on the FOPS.

This work shows that it is possible to produce any FOPS beam with high fidelity on a Si photonics platform. The equations derived from the specific design analyzed in detail here can be applied to any design of FOPS beam emitters, if it shares the generic feature of a microring resonator integrated with an angular grating of dipolar antennas. These results could be used in a range of applications, including microfluidic particle manipulation, as well as high-capacity, on-chip and free-space optical communications.

Funding. Engineering and Physical Sciences Research Council (EP/V000624/1); Royal Society (IEC\R3\183071, IES\R3\183086).

Optics EXPRESS

Acknowledgments. The authors acknowledge the use of the IRIDIS High Performance Computing Facility, and associated support services at the University of Southampton, in the completion of this work.

Disclosures. The authors declare no conflicts of interest.

Data availability. Following a period of embargo from the date of publication, the data that support the findings will be available in the University of Southampton's ePrints research repository.

Supplemental document. See Supplement 1 for supporting content.

References

1. H. Rubinsztein-Dunlop, A. Forbes, M. V. Berry, M. R. Dennis, D. L. Andrews, M. Mansuripur, C. Denz, C. Alpmann, P. Banzer, and T. Bauer, "Roadmap on structured light," J. Opt. **19**(1), 013001 (2017).
2. J. Bert, E. Prost, I. Tutunnikov, P. Béjot, E. Hertz, F. Billard, B. Lavorel, U. Steinitz, I. S. Averbukh, and O. Faucher, "Optical imaging of coherent molecular rotors," Laser & Photonics Reviews **14**(5), 1900344 (2020).
3. L. Novotny, M. Beversluis, K. Youngworth, and T. Brown, "Longitudinal field modes probed by single molecules," Phys. Rev. Lett. **86**(23), 5251–5254 (2001).
4. K. Toyoda, F. Takahashi, S. Takizawa, Y. Tokizane, K. Miyamoto, R. Morita, and T. Omatsu, "Transfer of light helicity to nanostructures," Phys. Rev. Lett. **110**(14), 143603 (2013).
5. J. Hamazaki, R. Morita, K. Chujo, Y. Kobayashi, S. Tanda, and T. Omatsu, "Optical-vortex laser ablation," Opt. Express **18**(3), 2144–2151 (2010).
6. V. Salakhutdinov, M. Sondermann, L. Carbone, E. Giacobino, A. Bramati, and G. Leuchs, "Optical trapping of nanoparticles by full solid-angle focusing," Optica **3**(11), 1181–1186 (2016).
7. M. Padgett and R. Bowman, "Tweezers with a twist," Nat. Photonics **5**(6), 343–348 (2011).
8. M. Liu, P. Huo, W. Zhu, C. Zhang, S. Zhang, M. Song, S. Zhang, Q. Zhou, L. Chen, and H. J. Lezec, "Broadband generation of perfect Poincaré beams via dielectric spin-multiplexed metasurface," Nat. Commun. **12**(1), 1–9 (2021).
9. Y. He, P. Wang, C. Wang, J. Liu, H. Ye, X. Zhou, Y. Li, S. Chen, X. Zhang, and D. Fan, "All-optical signal processing in structured light multiplexing with dielectric meta-optics," ACS Photonics **7**(1), 135–146 (2020).
10. V. Parigi, V. D'Ambrosio, C. Arnold, L. Marrucci, F. Sciarrino, and J. Laurat, "Storage and retrieval of vector beams of light in a multiple-degree-of-freedom quantum memory," Nat. Commun. **6**(1), 7706 (2015).
11. V. D'ambrosio, E. Nagali, S. P. Walborn, L. Aolita, S. Slussarenko, L. Marrucci, and F. Sciarrino, "Complete experimental toolbox for alignment-free quantum communication," Nat. Commun. **3**(1), 961 (2012).
12. G. Milione, H. Sztul, D. Nolan, and R. Alfano, "Higher-order Poincaré sphere, Stokes parameters, and the angular momentum of light," Phys. Rev. Lett. **107**(5), 053601 (2011).
13. C. Rosales-Guzmán, B. Ndagano, and A. Forbes, "A review of complex vector light fields and their applications," J. Opt. **20**(12), 123001 (2018).
14. Q. Zhan, "Cylindrical vector beams: from mathematical concepts to applications," Adv. Opt. Photonics **1**(1), 1–57 (2009).
15. D. Naidoo, F. S. Roux, A. Dudley, I. Litvin, B. Piccirillo, L. Marrucci, and A. Forbes, "Controlled generation of higher-order Poincaré sphere beams from a laser," Nat. Photonics **10**(5), 327–332 (2016).
16. H. Sroor, Y.-W. Huang, B. Sephton, D. Naidoo, A. Valles, V. Ginis, C.-W. Qiu, A. Ambrosio, F. Capasso, and A. Forbes, "High-purity orbital angular momentum states from a visible metasurface laser," Nat. Photonics **14**(8), 498–503 (2020).
17. S. Chen, X. Zhou, Y. Liu, X. Ling, H. Luo, and S. Wen, "Generation of arbitrary cylindrical vector beams on the higher order Poincaré sphere," Opt. Lett. **39**(18), 5274–5276 (2014).
18. J. Mendoza-Hernández, M. F. Ferrer-Garcia, J. A. Rojas-Santana, and D. Lopez-Mago, "Cylindrical vector beam generator using a two-element interferometer," Opt. Express **27**(22), 31810–31819 (2019).
19. M. M. Sánchez-López, J. A. Davis, N. Hashimoto, I. Moreno, E. Hurtado, K. Badham, A. Tanabe, and S. W. Delaney, "Performance of a q-plate tunable retarder in reflection for the switchable generation of both first-and second-order vector beams," Opt. Lett. **41**(1), 13–16 (2016).
20. P. Chen, S.-J. Ge, W. Duan, B.-Y. Wei, G.-X. Cui, W. Hu, and Y.-Q. Lu, "Digitalized geometric phases for parallel optical spin and orbital angular momentum encoding," ACS Photonics **4**(6), 1333–1338 (2017).
21. W. Han, Y. Yang, W. Cheng, and Q. Zhan, "Vectorial optical field generator for the creation of arbitrarily complex fields," Opt. Express **21**(18), 20692–20706 (2013).
22. J. Jia, K. Zhang, G. Hu, M. Hu, T. Tong, Q. Mu, H. Gao, F. Li, C.-W. Qiu, and P. Zhang, "Arbitrary cylindrical vector beam generation enabled by polarization-selective Gouy phase shifter," Photonics Res. **9**(6), 1048–1054 (2021).
23. X. Yi, X. Ling, Z. Zhang, Y. Li, X. Zhou, Y. Liu, S. Chen, H. Luo, and S. Wen, "Generation of cylindrical vector vortex beams by two cascaded metasurfaces," Opt. Express **22**(14), 17207–17215 (2014).
24. F. Yue, D. Wen, C. Zhang, B. D. Gerardot, W. Wang, S. Zhang, and X. Chen, "Multichannel polarization-controllable superpositions of orbital angular momentum states," Adv. Mater. **29**(15), 1603838 (2017).
25. W. Shu, X. Ling, X. Fu, Y. Liu, Y. Ke, and H. Luo, "Polarization evolution of vector beams generated by q-plates," Photonics Res. **5**(2), 64–72 (2017).
26. L. Feng, Y. Li, S. Wu, X. Guan, C. Yang, W. Tong, W. Li, J. Qiu, X. Hong, and Y. Zuo, "All-fiber generation of arbitrary cylindrical vector beams on the first-order Poincaré sphere," Photonics Res. **8**(8), 1268–1277 (2020).

Optics EXPRESS

27. X. Cai, J. Wang, M. J. Strain, B. Johnson-Morris, J. Zhu, M. Sorel, J. L. O'Brien, M. G. Thompson, and S. Yu, "Integrated Compact Optical Vortex Beam Emitters," Science **338**(6105), 363–366 (2012).
28. P. Miao, Z. Zhang, J. Sun, W. Walasik, S. Longhi, N. M. Litchinitser, and L. Feng, "Orbital angular momentum microlaser," Science **353**(6298), 464–467 (2016).
29. Z. Shao, J. Zhu, Y. Chen, Y. Zhang, and S. Yu, "Spin-orbit interaction of light induced by transverse spin angular momentum engineering," Nat. Commun. **9**(1), 926 (2018).
30. Z. Shao, J. Zhu, Y. Zhang, Y. Chen, and S. Yu, "On-chip switchable radially and azimuthally polarized vortex beam generation," Opt. Lett. **43**(6), 1263–1266 (2018).
31. H. Pi, T. Rahman, S. A. Boden, T. Ma, J. Yan, and X. Fang, "Integrated vortex beam emitter in the THz frequency range: Design and simulation," APL Photonics **5**(7), 076102 (2020).
32. Z. Zhang, X. Qiao, B. Midya, K. Liu, J. Sun, T. Wu, W. Liu, R. Agarwal, J. M. Jornet, and S. Longhi, "Tunable topological charge vortex microlaser," Science **368**(6492), 760–763 (2020).
33. K. V. G. Cognée, H. M. Doeleman, P. Lalanne, and A. F. Koenderink, "Generation of Pure OAM Beams with a Single State of Polarization by Antenna-Decorated Microdisk Resonators," ACS Photonics **7**(11), 3049–3060 (2020).
34. W. Bogaerts, P. De Heyn, T. Van Vaerenbergh, K. De Vos, S. K. Selvaraja, T. Claes, P. Dumon, P. Bienstman, D. Van Thourhout, and R. Baets, "Silicon microring resonators," Laser & Photon. Rev. **6**(1), 47–73 (2012).
35. D. Thomson, A. Zilkie, J. E. Bowers, T. Komljenovic, G. T. Reed, L. Vivien, D. Marris-Morini, E. Cassan, L. Virot, and J.-M. Fédéli, "Roadmap on silicon photonics," J. Opt. **18**(7), 073003 (2016).
36. E. D. Palik, *Handbook of optical constants of solids*, (Academic press, 1998).
37. M. J. Strain, X. Cai, J. Wang, J. Zhu, D. B. Phillips, L. Chen, M. Lopez-Garcia, J. L. O'Brien, M. G. Thompson, and M. Sorel, "Fast electrical switching of orbital angular momentum modes using ultra-compact integrated vortex emitters," Nat. Commun. **5**(1), 4856 (2014).
38. I. Moreno, J. A. Davis, I. Ruiz, and D. M. Cottrell, "Decomposition of radially and azimuthally polarized beams using a circular-polarization and vortex-sensing diffraction grating," Opt. Express **18**(7), 7173–7183 (2010).
39. J. D. Jackson, *Classical electrodynamics*, (Wiley, 1999).
40. J. Zhu, X. Cai, Y. Chen, and S. Yu, "Theoretical model for angular grating-based integrated optical vortex beam emitters," Opt. Lett. **38**(8), 1343–1345 (2013).